Bragg-edge neutron transmission spectrum analysis using a high-speed-camera-type time-of-flight neutron imaging detector

Hirotaka Sato[1,*], Koh-ichi Mochiki[2], Kenta Tanaka[2], Ken Ishizuka[2], Hirotaku Ishikawa[1], Takashi Kamiyama[1] and Yoshiaki Kiyanagi[3]

[1]Graduate School of Engineering, Hokkaido University, Kita-13 Nishi-8, Kita-ku, Sapporo 060-8628, Japan
[2]Graduate School of Engineering, Tokyo City University, 1-28-1 Tamatutumi, Setagaya-ku, Tokyo 158-8557, Japan
[3]Graduate School of Engineering, Nagoya University, Furo-cho, Chikusa-ku, Nagoya 464-8603, Japan

*Corresponding author. Tel.: +81-11-706-6679; Fax: +81-11-706-6679.
E-mail address: h.sato@eng.hokudai.ac.jp

Abstract

Thus far, quantitative imaging of crystallographic information using a time-of-flight (TOF) neutron Bragg-edge transmission method has been performed using counting-type neutron TOF-imaging detectors. However, at intense pulsed neutron beam facilities, the limit of the maximum counting rate of the detectors restricts acceptable neutron intensity. A camera-type neutron imaging detector can accept considerably higher neutron intensity than counting-type detectors. For this reason, a camera-type detector applicable for the TOF measurement has been developed. However, the camera-type detector has not been applied to quantitative analysis of crystallographic information thus far. As the neutron spectrum data obtained by a camera-type detector may have different characteristics compared with those obtained by a counting-type detector, it is important to experimentally demonstrate the applicability of the camera-type detector for quantitative crystallographic analysis. Thus, in this study, we performed a demonstration experiment using a steel knife specimen at a beam-line connected to a coupled-type neutron moderator of the Hokkaido University Neutron Source (HUNS). We applied the Rietveld-type data analysis method to measured Bragg-edge neutron transmission spectra in order to obtain quantitative crystallographic information, and we then conducted the crystalline phase imaging. Finally, using the new detector system along with the spectral analysis, the results were obtained non-destructively; the results showed that the crystalline phase

distribution of the steel knife composed of two phases was changed gradually, and the crystallographic texture and crystallite size distributions were almost uniform. In addition, the new detector system provided the best spatial resolution of 520 μm at a field-of-view of 13 cm × 13 cm.

Keywords: Time-of-flight neutron imaging detector; High speed camera; Pulsed neutron Bragg-edge transmission imaging; Quantitative crystallographic information analysis

1. Introduction

Pulsed neutron Bragg-edge transmission imaging using the time-of-flight (TOF) method is a unique material characterization tool that can simultaneously visualize quantitative crystallographic information in a bulk material over a large area with spatial resolution [1-6]. Therefore, construction projects of energy-resolved neutron imaging instruments at accelerator-driven intense pulsed spallation sources are in progress, e.g., J-PARC MLF BL22 "RADEN" [7], RAL ISIS-TS2 "IMAT" [8] and ESS "ODIN" [9]. However, at intense beam facilities, the limit of the maximum counting rate of counting-type neutron TOF-imaging detectors, such as the scintillator pixel type [10], gas electron multiplier (GEM) type [11], micro-pixel chamber (μPIC) type [12] and micro-channel plate (MCP) type [13], is not sufficient for measuring neutron transmission TOF spectra toward the full open beam.

For this reason, camera-type detectors, which are currently used at nuclear reactor-based intense neutron sources, are expected. Of course, for measuring neutron transmission TOF spectra, the camera should have a characteristic of a high frame rate (high-speed camera [14]) of the 10,000-fps class. However, as the volume of image data becomes immense, conducting long duration experiments is challenging. Thus, in a previous study [15], we developed a new neutron TOF-imaging detector equipped with a new high-speed camera system combined with the neutron color image intensifier [16]. This camera has a seamless accumulation system that can reduce the volume of data by the image accumulator, and continuously store the data in the memory during the experiment. Using this system, the long-time measurement of approximately 100 hours is feasible. In addition, this detector is expected to achieve the finest pixel size of 520 μm and a field-of-view (FOV) of 13 cm × 13 cm in Bragg-edge neutron transmission imaging experiments, which are better than those achieved by the GEM detector (pixel size of 800 μm and FOV of 10 cm × 10 cm). Furthermore, recently, higher spatial resolution techniques for this camera-type detector, namely, center-of-gravity calculation and super-resolution processing, have been developed [17].

However, one of the important final goals of neutron TOF-imaging experiments is actual quantitative evaluation of material information through neutron transmission spectrum analysis. For this purpose, in this study, we conducted an experiment to measure a steel knife specimen by using this camera system at a beam-line connected to a pulsed neutron source based on a coupled-type neutron moderator [18] and driven by a compact electron accelerator, the Hokkaido University Neutron Source (HUNS) [19]. Then, crystalline phase analyses with texture/extinction corrections using the Bragg-edge neutron transmission spectrum analysis program, RITS [2,20,21], were performed to demonstrate the applicability of the new camera-type detector. As a result, we could successfully obtain detailed information of the knife specimen by using this detector through spectrum analysis. In this paper, we report the details of the experiment and the data analysis.

2. High-speed camera detector for time-of-flight neutron imaging

To conduct efficient neutron TOF-imaging experiments using camera-type detectors, two important requirements must be considered. One is neutron and optical image intensifiers to obtain sufficient brightness at every neutron pulse. The other is a seamless accumulation system for many neutron images of the same TOF channel obtained during the long duration of irradiation. In this section, details of the implementation of both the image intensifiers and the seamless accumulation system in the new high-speed camera system are presented.

Fig. 1 presents a schematic layout of the high-frame-rate CMOS camera system combined with the neutron color image intensifier. The neutron color image intensifier [16] used in this system was TCN9100B made by TOSHIBA. The maximum FOV was 22.86 cm diameter, and the best achievable spatial resolution was < 30 μm. The input window for neutron-electron conversion was prepared with B_4C, comprising 99.7% enriched ^{10}B. The electrons were focused on the output window using an electron lens, and then the visible light was emitted from the output window. The FOV of the input window detected by the output window using the electron lens can be selected from three diameters, namely, 22.86, 17.78, 13.97 cm. The output window consisted of a short afterglow phosphor, Y_2SiO_5:Ce (with a decay time of 5 μs). This neutron image intensifier had a high-speed gating function to avoid burst neutron/gamma-ray flashes emitted from a neutron source.

Through the optical mirror and lens, the optical image was intensified by the optical image intensifier C9547-02 MOD using an MCP with a short afterglow phosphor P46 (HAMAMATSU). This optical image intensifier also had a high-speed gating function to avoid extremely bright images caused by burst neutron/gamma-ray flashes emitted from a neutron source. Through the optical mirror and lens, the optical image was captured by a high-frame-rate CMOS camera, MEMRECAM ST-821-HX (NAC Image Technology).

In this camera-type neutron TOF-imaging system, the pixel size and time resolution can be selected in principle as follows:

1. The number of pixels is 320 × 240 (572 μm pixel size in a 22.86 cm diameter FOV and 349 μm pixel size in a 13.97 cm diameter FOV) in case the time resolution is 10 μs (100 kfps mode).
2. The number of pixels is 512 × 512 (316 μm pixel size in a 22.86 cm diameter FOV and 193 μm pixel size in a 13.97 cm diameter FOV) in case the time resolution is 33.3 μs (30 kfps mode).
3. The number of pixels is 960 × 960 (169 μm pixel size in a 22.86 cm diameter FOV and 103 μm pixel size in a 13.97 cm diameter FOV) in case the time resolution is 100 μs (10 kfps mode).

The demonstration experiment presented in this paper was conducted in the second mode (30 kfps mode). The timings of both the accelerator (pulsed neutron source) and the camera (pulsed neutron TOF-imaging detector) were controlled under the same trigger control system.

Finally, details of the seamless accumulation system for the high-speed camera are presented. This system has a specialized image accumulation system (the frame integration unit in Fig. 1). Concretely, a certain TOF-channel image that is accumulated by 4096 neutron pulses has a 24-bit data length. Therefore, for example, in case the 100 kfps mode (the highest capturing speed) is used at an accelerator facility of 50 pulses per second such as HUNS, the data length becomes 24 bit × 2,000 (100,000 / 50 = 2,000 frames per pulse) in 82 seconds (4,096 / 50 = 82). The data length of 24 bit × 2,000 corresponds to a data file of 3,570 Mbit. A data volume of 44 Mbit/s (= 3,570 Mbit / 82 seconds), which corresponds to 5.6 MByte/s in this system, is continuously generated. However, as this system has a 2 TByte memory, the capturing of images continuously (seamlessly) for approximately 100 hours is feasible; 100 hours is usually sufficient for Bragg-edge transmission imaging experiments.

The neutron transmission TOF spectrum of a certain pixel, $Tr(tof)$, is obtained by the following calculation:

$$Tr(tof) = \frac{I_{\mathrm{sample}}(tof) - I_{\mathrm{dark}}(tof)}{I_{\mathrm{direct}}(tof) - I_{\mathrm{dark}}(tof)} .$$

Here, $I_{\mathrm{sample}}(tof)$ is the TOF-dependent signal measured with the sample in a neutron beam, $I_{\mathrm{direct}}(tof)$ is the TOF-dependent signal measured without the sample in a neutron beam, and $I_{\mathrm{dark}}(tof)$ is the TOF-dependent signal measured without neutron production.

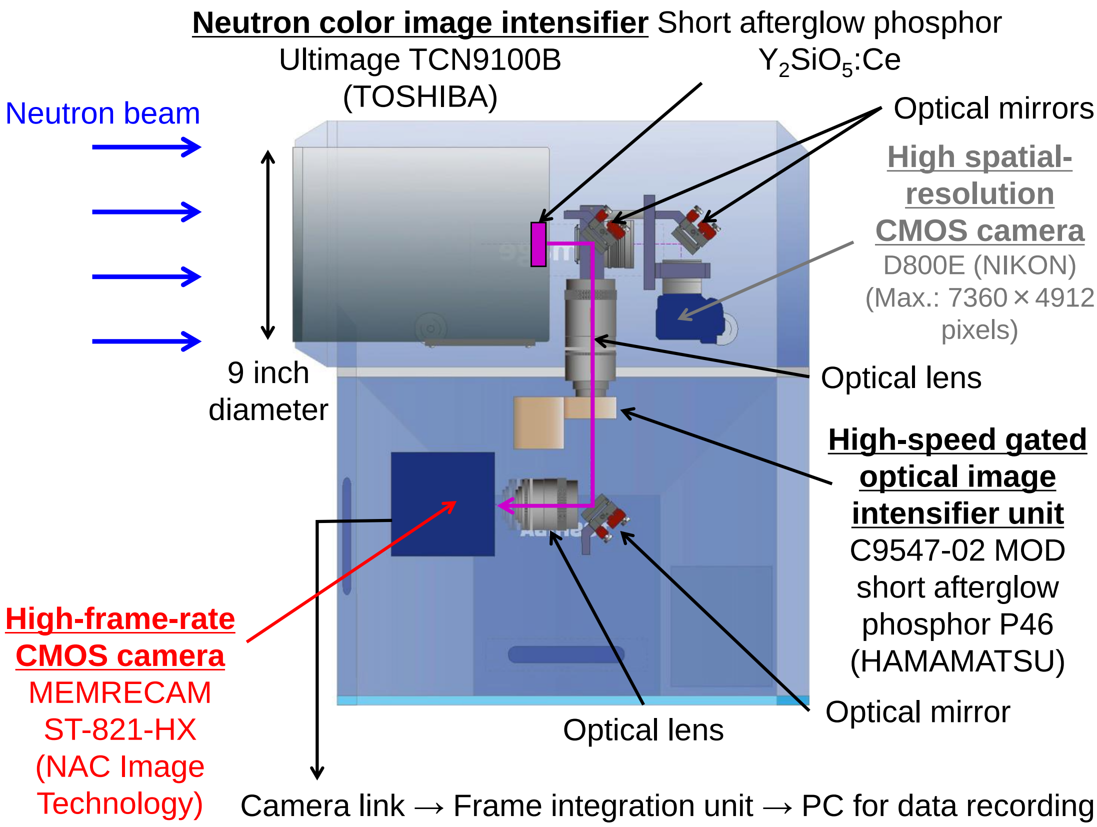

Fig. 1. Configuration of the neutron color image intensifier and the high-frame-rate CMOS camera with the seamless accumulation function for a time-of-flight neutron transmission imaging experiment.

3. Neutron TOF-imaging experiment

3.1. Experimental setup and conditions at the Hokkaido University Neutron Source

In this study, we used a relatively weak pulsed neutron source, the Hokkaido University Neutron Source (HUNS). We adopted the HUNS facility in this study for the following reasons: The main reason is to avoid the radio-activation of the new detector system before completion of the feasibility study. The second reason is that HUNS is one of the pioneering and reliable facilities and its facility has been used many times for the Bragg-edge neutron transmission imaging. The third reason is that the experiment would be successfully performed at intense pulsed neutron sources if the experiment could be done at the relatively weak pulsed neutron source.

The experimental setup was very simple, and quite similar to a layout described in Ref. [22]. Here, the key parameters are presented.

Fig. 2 shows a schematic layout of the neutron TOF-imaging experiment performed in this study. The experiment was performed at HUNS installed at the 1-kW class electron linear accelerator facility (Hokkaido LINAC) at Hokkaido University in Japan [19]. The pulse width of the electron beam was 3 μs, and the pulse repetition rate used was 50 Hz. Neutrons were generated through photonuclear reactions. The number of generated fast neutrons emitted from the neutron production target was approximately 10^{12} n/s. The generated fast neutrons were moderated to cold neutrons in a 20 K mesitylene-based main-moderator (5 cm thickness, 10 cm × 10 cm area) surrounded by polyethylene pre-moderators of 1.5 cm thickness. The graphite (inside) and lead (outside) reflectors surrounded the outside of moderators. A wing geometry was used in an arrangement between a target and a moderator in order to suitably secure the line-of-sight. Here, we used a coupled-type moderator to obtain higher cold neutron intensity [18]. As a result, a broad neutron pulse was emitted from the neutron source; about 170 μs in the pulse FWHM for cold neutrons. The moderated neutrons were transported to the sample/detector position through an evacuated tube of 3 m length. The total flight path length of neutrons was 5.8 m. The neutron flux at the detector position was approximately 10^4 n/cm^2/s. The wavelength resolution at the wavelength region of cold neutrons was 3%, which was not high wavelength resolution compared with that obtained for an instrument at a long flight path length viewing a decoupled-type moderator. The collimator ratio, L/D, was approximately 58 (17 mrad in the beam angular divergence) because there were no pinhole collimators in the beam-line. The beam size became larger than 10 cm × 10 cm (the moderator surface area) due to the divergence.

The neutron image intensifier (NII) combined with a high-speed camera system was operated in the 22.86 cm diameter FOV NII-mode with the 30 kfps camera-mode (number of pixels was 512 × 512, and the time resolution was 33.3 μs). In fact, for the reduction of statistical errors, crystalline phase analysis/imaging using the Rietveld-type spectral fitting analysis was performed in 256 × 256 pixels and the 66.6 μs TOF channel width. In conclusion, after the measurement, we found that the actual achieved pixel size was 520 μm and FOV was 13.3 cm × 13.3 cm. In any case, the pixel size is the finest in such large FOV condition for the measurement of Bragg-edge transmission imaging at pulsed neutron sources.

To reduce burst gamma-ray flashes, we set a lead plate of 1.7 cm thickness in the beam-line. In addition, to avoid burst neutron/gamma-ray flashes, the NII was operated from 1 ms to 11 ms after the burst (neutron wavelength region 0.07-0.75 nm). The optical image intensifier was operated from 2 ms to 7 ms after the burst (neutron wavelength region 0.14-0.48 nm, which is an actual usable neutron wavelength range).

The measurement time of an open beam for data normalization was 12 hours, and the measurement time of an in-sample beam was 15 hours. These values were normal for the pulsed neutron Bragg-edge transmission imaging at HUNS. The specimen was directly coupled to the imaging detector.

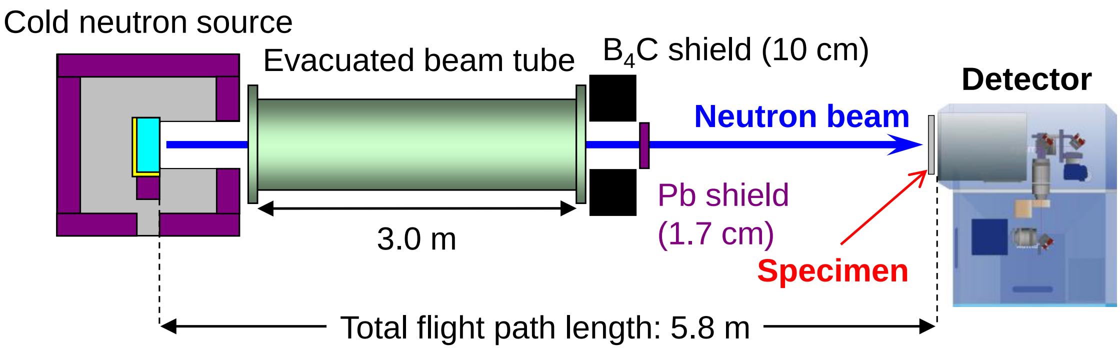

Fig. 2. Schematic layout of the neutron TOF-imaging experiment.

3.2. Specimen

Fig. 3 (a) shows a photograph of the specimen, which was a kitchen knife "Seki-no-magoroku" made in Japan. Here, we aimed to study the feasibility of the new detector system through a spectral analysis of Bragg-edge neutron transmission imaging. The analysis can provide the crystallographic texture and crystallite size of each crystalline phase at the wavelength resolution used in this study, and crystal lattice strain at a higher wavelength resolution of several times of 0.1%. Thus, we analyzed the full information at the wavelength resolution used in this study, namely, the crystallographic textures and crystallite sizes of two crystalline phases. We chose a new suitable specimen for this purpose. This knife specimen was suitable because it consisted of two crystalline phases according to X-ray diffraction measurements performed using D8 DISCOVER with GADDS (BRUKER AXS) with a cobalt Kα1 target (0.1789 nm wavelength) and a 0.8 mm tungsten collimator. Two irradiation points (with a spot size approximately 1 mm^2) were studied at one side and the reverse side of the knife. The results indicate that this knife consists of two crystalline phases of iron; α-Fe phase (BCC: body-centered cubic crystal structure) and γ-Fe phase (FCC: face-centered cubic crystal structure). In addition, different quantities of each phase between one side and the reverse side of the specimen were observed; one side consists of only α-Fe, and the other side consists of both α-Fe and γ-Fe (see Fig. 3 (b)). Thus, the X-ray diffraction studies revealed that we can demonstrate the feasibility of the new camera-type TOF-imaging detector toward quantitative imaging of crystalline phases (as well as their crystallographic textures and crystallite sizes) by using this complex steel sample.

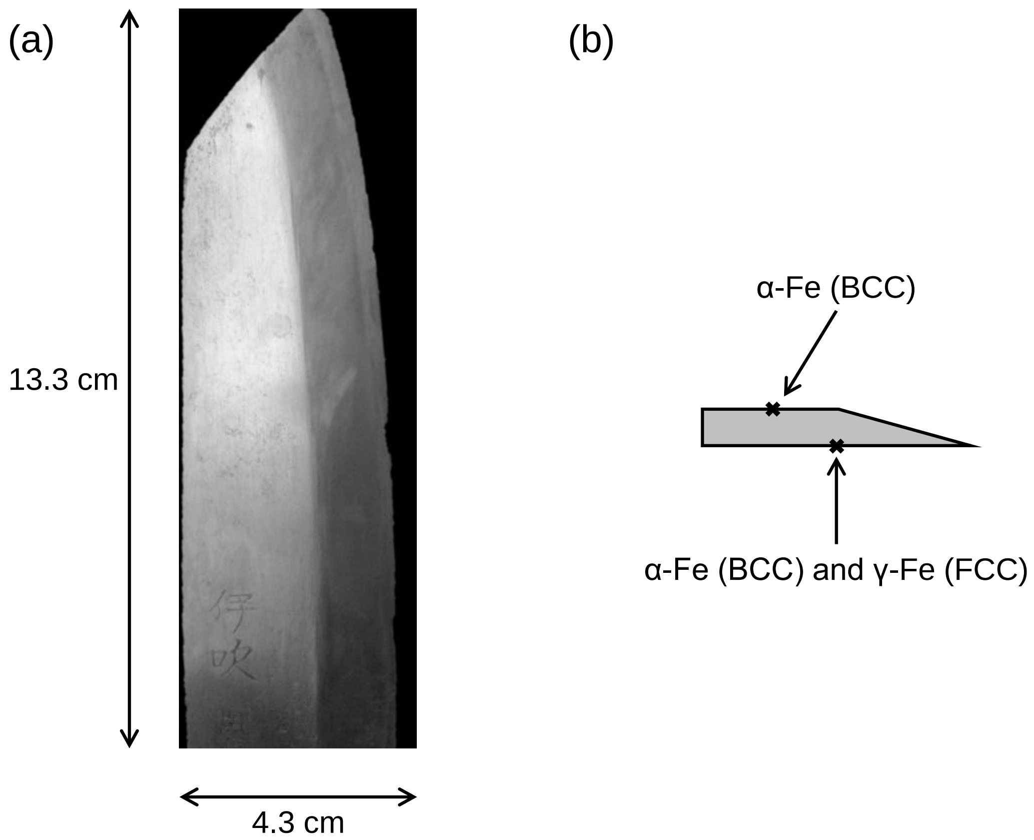

Fig. 3. (a) Photograph of the kitchen knife "Seki-no-magoroku" sample. (b) Cross-sectional picture of the sample. This sample contains two crystalline phases, α-Fe (BCC) and γ-Fe (FCC).

4. Results and discussion

In the experiment conducted in this study, the ratio of $I_{\mathrm{direct}}(tof)$ to $I_{\mathrm{dark}}(tof)$ was 1.004 at the neutron wavelength of 0.2 nm due to low neutron flux. The neutron transmission evaluated by pixels at the direct beam region successfully corresponded to 1.0. The statistical error was approximately 2% for a single TOF channel (66.6 μs) of a single pixel (520 μm). Further detailed evaluations about measured neutron transmission spectra are discussed in Sec. 4.2. In the following sections, we describe the experimental and analysis results in more detail.

4.1. Neutron transmission image

Fig. 4 shows a conventional white neutron radiograph. This image was visualized in a pixel size of 260 μm (number of pixels was 512 × 512). The FOV was 13.3 cm × 13.3 cm. We observe that the sample thickness decreases near the cutting edge.

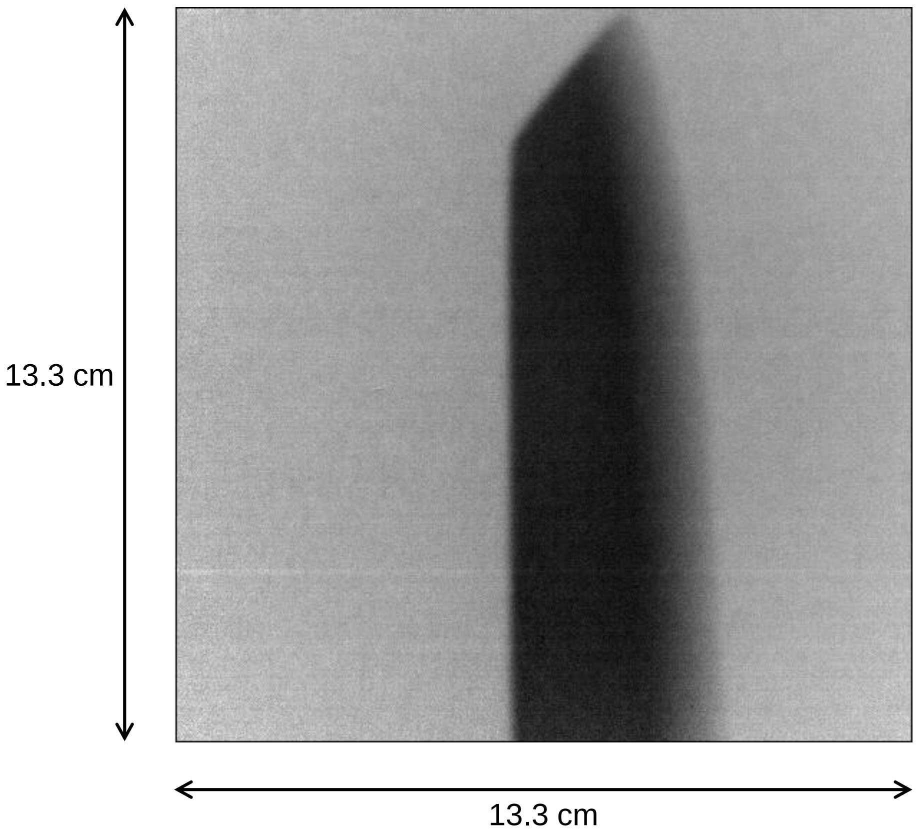

Fig. 4. White neutron radiograph of the kitchen knife sample, obtained by the present imaging detector. The pixel size is 260 μm, and the number of pixels is 512 × 512.

4.2. Bragg-edge neutron transmission spectrum and its Rietveld-type analysis

We observed and analyzed the Bragg-edge neutron transmission spectra of the blade body and the cutting edge of the knife sample. Fig. 5 shows the Bragg-edge neutron transmission spectra of (a) the thick blade body and (b) the thin cutting edge, measured by some pixels' summation of the high-speed camera detector. Note that Bragg-edges are broadened due to the low wavelength resolution caused by the coupled moderator (see Ref. [22]).

First, we clearly observe two Bragg-edges at wavelengths 0.36 nm and 0.41 nm. The candidates of the 0.41 nm Bragg-edge are α-Fe (BCC) {110} (0.405 nm) and γ-Fe (FCC) {111} (0.41 nm). By contrast, the candidate of the 0.36 nm Bragg-edge is only γ-Fe {200} (0.36 nm). Therefore, we conducted the profile fitting analysis based on γ-Fe. The Rietveld-type fitting analysis program that we used here was Rietveld Imaging of Transmission Spectra (RITS) [2,20,21]. The instrumental resolution function in the RITS program, which expresses Bragg-edge broadening due to the low wavelength resolution, had the same parameters previously obtained by an experiment conducted using a counting-type neutron detector (GEM-type detector [11]) at the same beam-line. As expected, profile fitting based on the single phase (γ-Fe) could not reconstruct the experimental transmission intensities over the wide wavelength bandwidth (see solid single-lines (FCC fitting) in Fig. 5). Next, we assumed the double phases, γ-Fe and α-Fe, as expected by X-ray diffraction studies. The solid double-lines (FCC + BCC fitting) in Fig. 5 show the profile fitting curves. In particular, Fig. 5 (a) clearly indicates that this assumption could well reconstruct the experimental transmission intensities over the wide wavelength bandwidth. This implies that Bragg-edge neutron transmission spectra measured by this camera system can successfully identify the existence of each crystalline phase in a material composed of multiple phases.

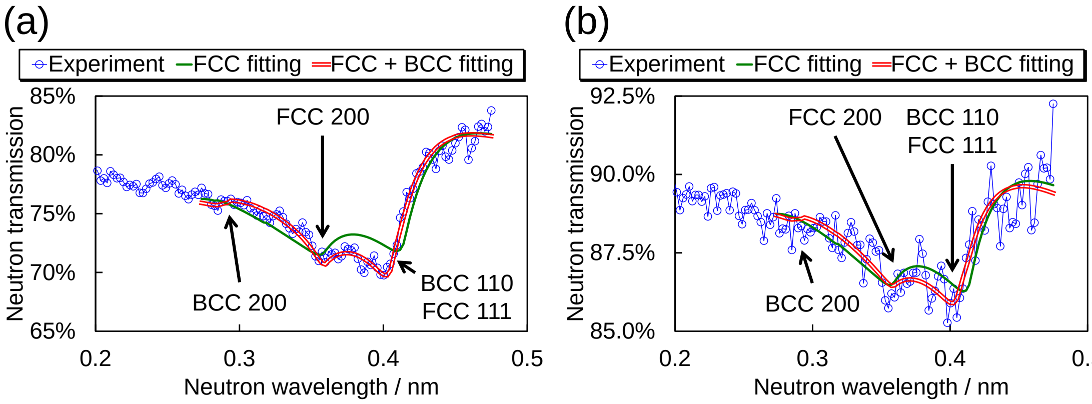

Fig. 5. Bragg-edge neutron transmission spectra measured by some pixels' summation of the present imaging detector. The fitting curves were given by the RITS program. (a) Thick blade body. (b) Thin cutting edge. The FCC and BCC double-phase assumption can give a better fitting curve. Incidentally, fluctuations of the experimental data of Fig. 5 (b) were caused by statistical errors. The fluctuations are emphasized due to enlargement of the vertical axis of Fig. 5 (b) (the plotted range is 7.5%) compared with that of Fig. 5 (a) (the plotted range is 20%). The relative errors for both the data are almost the same, 0.6%-0.7%.

4.3. Crystalline phase imaging with texture and extinction corrections

By the transmission-spectrum profile fitting analyses over all pixels using the RITS program, quantitative images of each phase were obtained under the correction of both the texture effect and extinction effect [20]. This is because RITS has the March-Dollase preferred orientation function for the texture analysis and Sabine's primary extinction function for the crystallite size analysis [2].

Figs. 6 (a) and (b) show the crystalline phase imaging results of α-Fe (BCC) and γ-Fe (FCC), respectively. The imaging results were expressed by the projected atomic number density (atomic number density × thickness) for each phase. Furthermore, by using this value, the volume fraction of each phase can be derived [23].

Fig. 6 (a) indicates that the projected atomic number density of α-Fe reduces gradually from the blade body to the cutting edge. This trend is similar to the result of the white neutron radiograph (see Fig. 4). By contrast, the projected atomic number density of γ-Fe does not change over the whole region. At the blade body region, the projected atomic number density of γ-Fe is almost a half (0.8×10^{22} cm^{-2}) of that of α-Fe (1.9×10^{22} cm^{-2}). Meanwhile, at the cutting edge region, the projected atomic number densities of both phases are almost the same (~ 0.9×10^{22} cm^{-2}). It is also interesting that γ-Fe is not present at all at the tip of the cutting edge (see the top-center region (a region indicated by a white arrow) of Fig. 6 (b)).

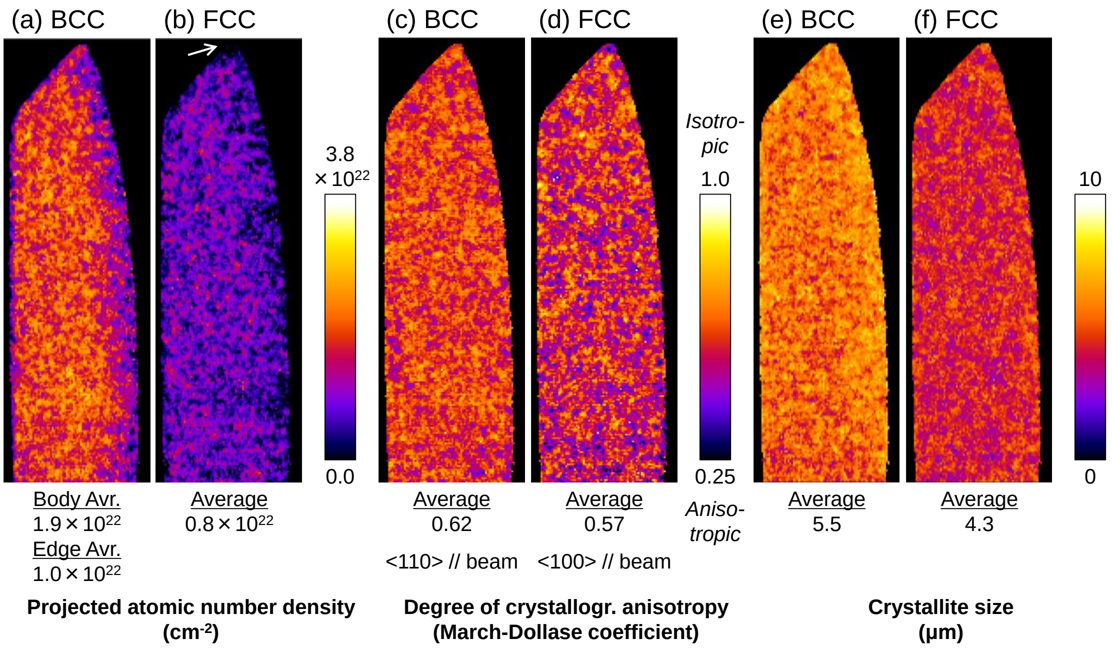

Fig. 6. Quantitative imaging results of (a) α-Fe (BCC) phase and (b) γ-Fe (FCC) phase. The projected atomic number density effectively indicates the thickness variations of each phase; quantitative texture imaging results of (c) α-Fe (BCC) phase and (d) γ-Fe (FCC) phase; crystallite size imaging results of (e) α-Fe (BCC) phase and (f) γ-Fe (FCC) phase; these were obtained with the latest RITS program [21]. In these images, the pixel size is 520 μm and the field-of-view is 13.3 cm × 4.3 cm.

4.4. Discussion of the whole knife structure based on phase, texture and crystallite-size imaging results

Figs. 6 (c) and (d) present the quantitative imaging results of crystallographic anisotropy of (c) α-Fe (BCC) phase and (d) γ-Fe (FCC) phase, expressed by the March-Dollase coefficient [2,24,25]. In addition, the RITS analyses suggested that the preferred orientations parallel to the neutron beam direction were <110> for α-Fe and <100> for γ-Fe. Figs. 6 (e) and (f) show crystallite size imaging results of (e) α-Fe (BCC) phase and (f) γ-Fe (FCC) phase.

The most important point from both viewpoints of texture and crystallite size is that both microstructures of each phase are almost uniform over the whole sample volume. This trend is quite different from that of Japanese swords, which usually receive heat treatment and strain hardening during processing and have spatial variations in terms of texture and microstructure [26]. In other words, it can be deduced that the knife specimen we measured did not undergo such plastic deformation.

According to these discussions, we finally discovered the whole structure of the knife as follows. Fig. 7 shows a schematic layout of the deduced whole knife structure. First, this knife did not receive any heat treatment and strain hardening, as observed from Figs. 6 (c)-(f). At the cutting edge, α-Fe (BCC) and γ-Fe (FCC) exist in almost the same atomic quantity, as observed from Figs. 6 (a) and (b). From the edge to the body, only α-Fe (BCC) gradually increases, as seen in from Figs. 6 (a) and (b). Therefore, it is estimated that two types of steel plate are stacked to make this knife, as illustrated in Fig. 7. These estimations are consistent with the X-ray diffraction results presented in Fig. 3 (b). This confirms the reliability of the neutron experimental method using the present detector system. Furthermore, the composition of each phase was obtained by the neutron Bragg-edge transmission method, which could not be quantitatively obtained by the X-ray diffraction. This important result indicates the usability of neutron transmission spectrum analysis using the camera-type TOF-imaging neutron detector.

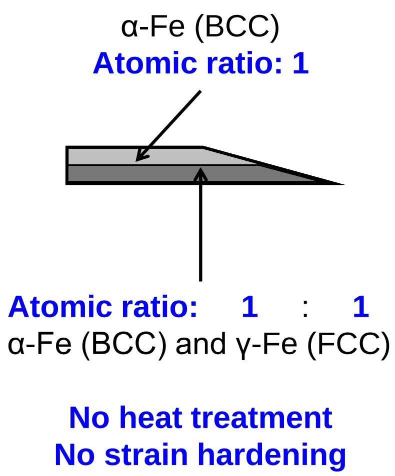

Fig. 7. A schematic layout of the whole structure of the knife specimen, as deduced from the phase, texture and crystallite size imaging results.

5. Conclusion

We successfully conducted the first demonstration of quantitative crystallographic information imaging using the time-of-flight (TOF) Bragg-edge transmission imaging by using a camera-type detector, namely, the neutron color image intensifier combined with a new high-speed camera system. The important point for the achievement is that the profile analysis of the neutron spectrum over a wide wavelength bandwidth of Bragg-edge transmission data (the Rietveld-type analysis) is feasible using this new detector. In addition, the crystalline phase imaging was achieved under the best spatial condition at the beam-line connected to the coupled-type moderator of the HUNS facility; the conditions were a 520 μm pixel size and a 13.3 cm × 13.3 cm field-of-view, which is larger than the field-of-view (less than 10 cm) of counting-type detectors.

In the future, the developed new detector system may achieve Bragg-edge neutron transmission imaging experiments of better performances at intense pulsed neutron sources. For example, imaging of 260 μm pixel size, short measurement time and high wavelength resolution (strain) analysis, would be further achieved with a 13.3 cm × 13.3 cm field-of-view.

Acknowledgements

The authors thank Mr. Koh-ichi Sato of Hokkaido University for accelerator operations and experimental assistances. This work was supported by JSPS KAKENHI Grant Number 23226018.

References

[1] J. R. Santisteban, L. Edwards, M. E. Fitzpatrick, A. Steuwer, P. J. Withers, M. R. Daymond, M. W. Johnson, N. Rhodes and E. M. Schooneveld, Nucl. Instrum. Methods A **481** (2002) 765-768.

[2] H. Sato, T. Kamiyama and Y. Kiyanagi, Mater. Trans. **52** (2011) 1294-1302.

[3] R. Woracek, D. Penumadu, N. Kardjilov, A. Hilger, M. Boin, J. Banhart and I. Manke, Adv. Mater. **26** (2014) 4069-4073.

[4] H. Sato, T. Sato, Y. Shiota, T. Kamiyama, A. S. Tremsin, M. Ohnuma and Y. Kiyanagi, Mater. Trans. **56** (2015) 1147-1152.

[5] H. Sato, Y. Shiota, T. Shinohara, T. Kamiyama, M. Ohnuma, M. Furusaka and Y. Kiyanagi, Phys. Procedia **69** (2015) 349-357.

[6] H. Sato, Y. Shiota, S. Morooka, Y. Todaka, N. Adachi, S. Sadamatsu, K. Oikawa, M. Harada, S. Y. Zhang, Y. H. Su, T. Kamiyama, M. Ohnuma, M. Furusaka, T. Shinohara and Y. Kiyanagi, J. Appl. Crystallogr. **50** (2017) 1601-1610.

[7] T. Shinohara, T. Kai, K. Oikawa, M. Segawa, M. Harada, T. Nakatani, M. Ooi, K.

Aizawa, H. Sato, T. Kamiyama, H. Yokota, T. Sera, K. Mochiki and Y. Kiyanagi, J. Phys. Conf. Ser. **746** (2016) 012007.

[8] W. Kockelmann, S. Y. Zhang, J. F. Kelleher, J. B. Nightingale, G. Burca and J. A. James, Phys. Procedia **43** (2013) 100-110.

[9] M. Strobl, Phys. Procedia **69** (2015) 18-26.

[10] H. Sato, O. Takada, S. Satoh, T. Kamiyama and Y. Kiyanagi, Nucl. Instrum. Methods A **623** (2010) 597-599.

[11] S. Uno, T. Uchida, M. Sekimoto, T. Murakami, K. Miyama, M. Shoji, E. Nakano, T. Koike, K. Morita, H. Satoh, T. Kamiyama and Y. Kiyanagi, Phys. Procedia **26** (2012) 142-152.

[12] J. D. Parker, M. Harada, K. Hattori, S. Iwaki, S. Kabuki, Y. Kishimoto, H. Kubo, S. Kurosawa, Y. Matsuoka, K. Miuchi, T. Mizumoto, H. Nishimura, T. Oku, T. Sawano, T. Shinohara, J. Suzuki, A. Takada, T. Tanimori and K. Ueno, Nucl. Instrum. Methods A **726** (2013) 155-161.

[13] A. S. Tremsin, J. B. McPhate, A. Steuwer, W. Kockelmann, A. M Paradowska, J. F. Kelleher, J. V. Vallerga, O. H. W. Siegmund and W. B. Feller, Strain **48** (2012) 296-305.

[14] M. Segawa, M. Ooi, T. Kai, T. Shinohara, H. Satoh and M. Kureta, JPS Conf. Proc. **8** (2015) 036006.

[15] K. Mochiki, K. Ishizuka, K. Morikawa, T. Kamiyama and Y. Kiyanagi, Phys. Procedia **69** (2015) 143-151.

[16] K. Nittoh, C. Konagai, T. Noji and K. Miyabe, Nucl. Instrum. Methods A **605** (2009) 107-110.

[17] T. Uragaki, J. Koide, J. Kawarabayashi, K. Mochiki, Y. Matsumoto, Y. H. Su, K. Hiroi, T. Shinohara and T. Kai, JPS Conf. Proc. **22** (2018) 011027.

[18] Y. Kiyanagi, N. Watanabe and H. Iwasa, Nucl. Instrum. Methods A **312** (1992) 561-570.

[19] M. Furusaka, H. Sato, T. Kamiyama, M. Ohnuma and Y. Kiyanagi, Phys. Procedia **60** (2014) 167-174.

[20] H. Sato, T. Shinohara, R. Kiyanagi, K. Aizawa, M. Ooi, M. Harada, K. Oikawa, F. Maekawa, K. Iwase, T. Kamiyama and Y. Kiyanagi, Phys. Procedia **43** (2013) 186-195.

[21] H. Sato, K. Watanabe, K. Kiyokawa, R. Kiyanagi, K. Y. Hara, T. Kamiyama, M. Furusaka, T. Shinohara and Y. Kiyanagi, Phys. Procedia **88** (2017) 322-330.

[22] H. Sato, Y. Shiota, T. Kamiyama, M. Ohnuma, M. Furusaka and Y. Kiyanagi, Phys. Procedia **60** (2014) 254-263.

[23] Y. H. Su, K. Oikawa, S. Harjo, T. Shinohara, T. Kai, M. Harada, K. Hiroi, S. Y. Zhang,

J. D. Parker, H. Sato, Y. Shiota, Y. Kiyanagi and Y. Tomota, Mater. Sci. Eng. A **675** (2016) 19-31.
[24] W. A. Dollase, J. Appl. Crystallogr. **19** (1986) 267-272.
[25] A. C. Larson and R. B. Von Dreele, *General Structure Analysis System (GSAS)*, Los Alamos National Laboratory Report LAUR 86-748, Los Alamos National Laboratory, Los Alamos (2004).
[26] Y. Shiota, H. Hasemi and Y. Kiyanagi, Phys. Procedia **88** (2017) 128-133.